Composition and Surface Properties of Transneptunian Objects and Centaurs

M. Antonietta Barucci
Observatoire de Paris

Michael E. Brown
California Institute of Technology

Joshua P. Emery
SETI Institute and NASA Ames Research Center

Frederic Merlin
Observatoire de Paris

Centaurs and transneptunian objects are among the most primitive bodies of the solar system and investigation of their surface composition provides constraints on the evolution of our planetary system. An overview of the surface properties based on space- and groundbased observations is presented. These objects have surfaces showing a very wide range of colors and spectral reflectances. Some objects show no diagnostic spectral bands, while others have spectra showing signatures of various ices (such as water, methane, methanol, and nitrogen). The diversity in the spectra suggests that these objects represent a substantial range of original bulk compositions, including ices, silicates, and organic solids. The methods to model surface compositions are presented and possible causes of the spectral diversity are discussed.

1. INTRODUCTION

The investigation of the surface composition of transneptunian objects (TNOs) and Centaurs provides essential information on the conditions in the early solar system at large distances from the Sun. The transneptunian and asteroid belts can be considered as the "archeological sites" where the nature of planet-building material may be examined. The investigation of the properties of these icy bodies, as remnants of the external planetesimal swarms, is essential to understanding the formation and the evolution of the population. The knowledge of the compositional nature of the whole population can provide constraints on the processes that dominated the evolution of the early solar nebula as well as of other planetary systems around young stars. Even though space weathering due to solar radiation, cosmic rays, and interplanetary dust can affect the uppermost surface layer of these bodies (see chapter by Hudson et al.), and energetic collisions could have played an important role (see chapter by Leinhardt et al.), TNOs represent the most pristine material available for groundbased investigation.

Studies of the physical properties of these objects are still limited by their faintness, and many open questions remain concerning their surface composition. Compositional determination remains a technically challenging practice for these astronomical targets. Several irregular satellites (see chapter by Nicholson et al.) seem to have a Kuiper belt origin. Some of these have been well studied, but their distinct histories preclude direct interpretation in terms of the transneptunian region. Pluto and its satellite Charon remain the best observed TNOs (see chapters by Stern and Trafton and Weaver et al.), although the system formation remains a puzzling question.

2. OBSERVATIONAL TECHNIQUES

Photometry has been the most extensively used technique to investigate the surface properties of these remote objects, since most of them are extremely faint. Many different photometric observations have been performed, particularly in the visible region, providing data for a large number of objects.

Photometric surveys have observed more than 130 objects and have revealed a very surprising color diversity. Various statistical analyses have been applied and a wide range of possible correlations between optical colors and physical and orbital parameters have been investigated (see chapters by Tegler et al. and Doressoundiram et al.).

Phase functions and polarimetry provide additional information on surface properties. The behavior of polarization phase angle depends on properties of the upper surface layer, such as albedo, particle size distribution, porosity,

heterogeneity, etc. These characteristics can be constrained through numerical modeling of light scattering by the surface material, taking into account the chemical and mineralogical composition (see chapter by Belskaya et al.). Measuring thermal fluxes in the far-infrared is also a fundamental technique for albedo determination (see chapter by Stansberry et al.).

However, these techniques can provide only limited constraints on the surface composition of the population. For instance, colors can be influenced not only by composition, but also by scattering effects in particulate regoliths and by viewing geometry. Colors cannot, in general, be used to determine composition, but they can be used to classify objects into groups. A new taxonomy based on color indices (B–V, V–R, V–I, V–J, V–H, and V–K) has been derived that identifies four groups: BB, BR, IR, and RR. The BB group contains objects with neutral colors, the RR group contains those with very red colors (the reddest among the solar system objects), and the other two groups have intermediate behaviors (*Barucci et al.,* 2005b; chapter by Fulchignoni et al.). The physical significance of color diversity is still unclear, although it is reasonable to assume that the different colors reflect intrinsically different composition and/or different evolutional history.

The most detailed information on the compositions of TNOs can be acquired only from spectroscopic observations. The wavelength range between 0.4 and 2.5 μm provides the most sensitive technique available from the ground to characterize the major mineral phases and ices present on TNOs. Diagnostic spectral features of silicate minerals, feldspar, carbonaceous assemblages, organics, and water-bearing minerals are present in the visible (V) and near-infrared (NIR) spectral regions. At the near-infrared wavelengths there are also signatures from ices and hydrocarbons. Cometary activity has been detected on several Centaurs (*Luu and Jewitt,* 1990; *Pravdo et al.,* 2001; *Fernandez et al.,* 2001; *Choi and Weissman,* 2006). Weakly active Centaurs or TNOs could also show fluorescent gaseous emission bands.

Most of the known TNOs and Centaurs are too faint for spectroscopic observations, even with the world's largest telescopes. As a result, only the brightest bodies have been observed spectroscopically. The exposure times required are generally long, and as the objects rotate around their maximum inertia principal axis, the resulting spectra often contain signals from both sides of the object.

2.1. Major Spectroscopy Ground Surveys

The brightest Centaurs can be observed with small telescopes, particularly for the V range, but fainter objects have required the use of 8–10-m-class telescopes. *Luu and Jewitt* (1996) were the first to observe these distant objects. They used the Keck 1 telescope, and have continued their program since that time with observations at the Keck and Subaru telescopes on Mauna Kea.

2.1.1. European Southern Observatory (ESO) survey. As soon as VLT-ESO began operating, *Barucci et al.* (2000) and the associated team started an observational campaign in the visible and near-infrared at unit 1 Antu, unit 3 Melipan, and unit 4 Yepun. To date, about 20 objects have been observed at VLT. For most of these objects, simultaneous V + NIR spectra were measured.

2.1.2. California Institute of Technology (Caltech) survey. *Brown* (2000) and collaborators started observations of TNOs and Centaurs with the low-resolution infrared spectrograph at the Keck Observatory. To date, about 30 objects have been observed at Keck in H + K band.

The observational strategies vary depending on the telescope and instrumentation. In general, a sequence of observations includes several spectra of the object, solar analogs, and a series of calibration that include bias frames, flat field, and a lamp for wavelength calibration. Careful removal of the dominant sky background (atmospheric emission bands) in the infrared and the choice of good solar analogs are essential steps to ensure high-quality data. The solar analog has to be observed during the same night at the same air mass as the target. Using large telescopes, the known good solar analogs generally are too bright and cannot be used as they could saturate the instruments. Simultaneous measures of the absolute calibration are essential to adjust the different spectral pass-bands and provide reliable final spectra.

2.2. Space Surveys

Although discovery and characterization of TNOs and Centaurs are dominated by groundbased measurements, several programs with both the Hubble and Spitzer Space Telescopes are also relevant. The Hubble programs span the visible and near-infrared, detecting sunlight reflected off the surfaces. Several authors have observed with Hubble; in particular, *Noll et al.* (2000) used NICMOS to measure broadband reflectances in the near-infrared ($\lambda < 2.5$ μm) of four TNOs. A near-infrared reflectance spectrum (1–2 μm) of the Centaur 8405 Asbolus was also measured using NICMOS on Hubble (*Kern et al.,* 2000).

The Spitzer Space Telescope (*Werner et al.,* 2004) allows low- and moderate-spectral-resolution spectroscopy from 5.2 to 38 μm. Broadband imaging photometry is also possible in nine bands from 3.6 to 160 μm. The lower end of this wavelength range is sensitive to reflected sunlight from the distant (cold) TNOs and Centaurs. At longer wavelengths, however, thermal emission radiated by the bodies themselves is detected. The crossover between reflected and emitted radiation depends on surface temperature and can occur anywhere from near 6 μm for some Centaurs to ~15 μm for colder TNOs. Thermal emission measurements with Spitzer can also be used to derive sizes and albedo (see chapter by Stansberry et al.). Furthermore, thermal emission spectra offer the opportunity to detect emissivity features, which are diagnostic of surface composition. Unfortunately, spectral measurements are less sensitive than broadband measurements, so only the thermally brightest TNOs and Centaurs can be usefully detected with the spectrograph on Spitzer.

Spitzer has a relatively short lifetime due to finite supplies of cryogen to cool the detectors, but several current and pending programs are taking advantage of Spitzer for TNO studies while it lasts.

3. SPECTROSCOPY RESULTS

3.1. The Visible Spectra

Visible spectra, generally obtained with a low-resolution grism, are mostly featureless with a large variation in the spectral gradient from neutral to very red, confirming the diversity seen in broadband colors. The visible wavelength range provides important constrains on surface composition, particularly for reddest objects, whose reflectance increases rapidly with wavelength. Such ultrared slopes are usually interpreted to indicate the presence of organic material on the surface. The measured spectral slopes range between –1%/10^3 Å and ~55%/10^3 Å, with the Centaurs Pholus and Nessus being the reddest objects known up to now in the solar system. The visible range is also important for detecting aqueously altered minerals such as phyllosilicates. Three objects, all Plutinos (Fig. 1), have had reports of broad absorptions present in their visible spectra. These features are very similar to those due to aqueously altered minerals found in spectra of some main-belt asteroids, irregular satellites, and meteorites (*Vilas and Gaffey,* 1989, and subsequent papers). In the case of the three Plutinos, however, all attempts to confirm these absorptions have shown only featureless spectra. While spectral variability due to rotational modulation cannot be excluded, these detections must remain uncertain until the observations are confirmed. The presence of phyllosilicates has also been suggested by *Jewitt and Luu* (2001), who reported absorption bands (around 1.4 and 1.9 μm) in the spectrum of the Centaur 26375 1999 DE_9. All these features are rather weak, and the reality of these bands also requires confirmation.

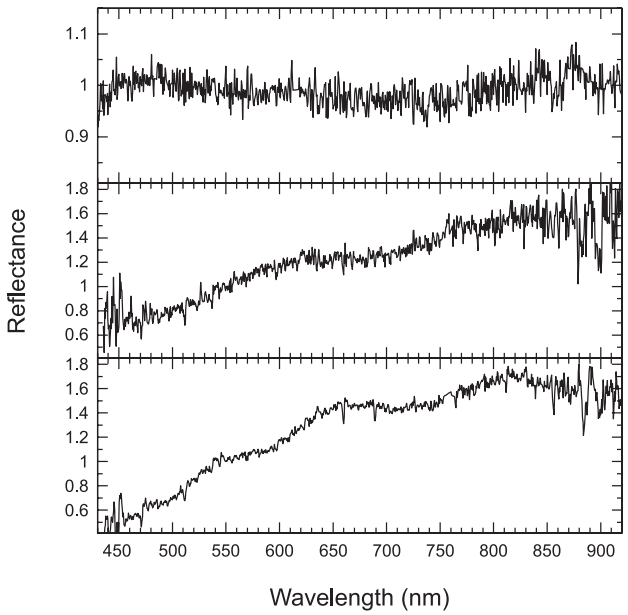

Fig. 1. Visible spectra of three TNOs showing aqueous alteration bands. The top spectrum of 2003 AZ_{84} was obtained by *Fornasier et al.* (2004b), and a continuum computed with a linear least-squares fit to the observed spectrum has been removed. The broad absorption band has been identified centered at about 700 nm. The other two spectra were obtained by *Lazzarin et al.* (2003). The 47932 (GN171) spectrum exhibits a feature around 725 nm, while 38628 Huya presents two absorption bands centered respectively at about 600 and 730 nm. On asteroids and meteorites these bands have been attributed to an $Fe^{2+} \rightarrow Fe^{3+}$ charge transfer in iron oxides in phyllosilicates (*Vilas and Gaffey,* 1989).

How aqueous alteration process could have occurred far from the Sun is not well understood, but formation of hydrated minerals directly in the early solar nebula cannot be excluded. Finding aqueously altered materials in TNOs would not be too surprising (*de Bergh et al.,* 2004), since hydrous materials seem to be present in comets, and hydrous silicates are detected in interplanetary dust particles (IDPs) and in micrometeorites.

3.2. Near-Infrared Spectra

The near-infrared wavelength range (1–2.5 μm) is the most diagnostic region for determining the presence of ices. Signatures of water ice are present at 1.5, 1.65, 2.0 μm, and signatures of other ices include those due to CH_4 around 1.7 and 2.3, CH_3OH at 2.27 μm, and NH_3 at 2 and 2.25 μm, as well as solid C-N bearing material at 2.2 μm. The first observations in this wavelength range were carried out on the Centaurs 2060 Chiron and 5145 Pholus (see *Barucci et al.,* 2002b, for a review on Centaurs) while the first spectrum of a TNO, 15789 (1993 SC), was obtained by *Luu and Jewitt* (1996) in the visible and by *Brown et al.* (1997) in the near-infrared. These early data showed a very noisy red dish spectrum with some features that they attributed to hydrocarbon ice, but that did not appear in higher-quality observations obtained later (*Jewitt and Luu,* 2001). In the near-infrared region some Centaur and TNO spectra are featureless, while others show signatures of ices. Reflectance spectra from 1.4 to 2.4 μm of four representative TNOs observed at Keck with various signal precision are reported in Fig. 2.

3.3. Results from Groundbased Spectroscopy

More than 40 objects have been observed spectroscopically to date, but only a few have been well studied in both the visible and near-infrared and rigorously modeled. These objects are faint and even observations with long exposure time and with the largest telescopes (Keck, Gemini, Subaru, and VLT) often do not yield high-quality spectra. All the objects observed spectroscopically in the near-infrared and available in literature have been listed in Table 1.

In Fig. 3 the visible and the near-infrared spectra of some Centaurs and TNOs observed at VLT are shown along with the best-fit spectral model. In general, TNOs and Centaurs

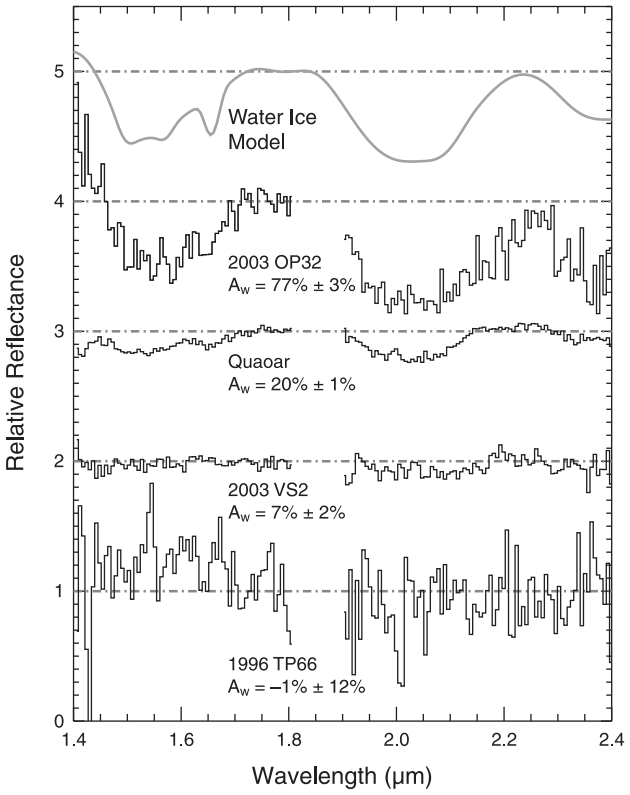

Fig. 2. The infrared reflectance spectra of four representative KBOs obtained with the Near Infrared Camera at the Keck Observatory. The spectra are normalized by the reflectance at 1.7 μm and are shifted by units of 1.0. The gray dashed lines mark the 0% and 100% relative reflectance for each spectrum. A model spectrum of pure water ice (smooth, gray line) created using a Hapke model and an ice temperature of 40 K with a grain size of 50 μm, is presented for comparison. The model shows the broad water ice absorptions at 1.5 and 2.0 μm that are also seen in the spectra of 2003 OP_{32} and Quaoar. The feature at 1.65 μm due to crystalline water ice feature is also seen in these spectra. The quantity A_w, quantifying the amount of water ice absorption at 2.0 μm, is reported next to each spectrum (see text for definition).

have similar spectral behavior. Both populations show a large diversity in spectra, which presumably indicates a similarly large diversity in surface characteristics. It is necessary to combine the visible and near-infrared spectra in order to place strong constraints on surface composition. However, in some cases this is not a sufficient step.

Radiative transfer models have been used to interpret the V + NIR spectra using intimate or geographical mixtures of organics, silicate minerals, carbonaceous assemblages, ices, and/or hydrocarbons. The red slopes are in general well reproduced by organic compounds like tholins or kerogen on the surface. The fractional abundance of these materials depends on the steepness of the spectral slope. Flat slopes and low-albedo objects can be well modeled with a large fraction of amorphous carbon. Silicates also seem to be present on some surface. For example, olivine on the surface of 5145 Pholus (*Cruikshank et al*., 1998) significantly improves the model fit when included. Ices are easily detected when high-quality spectra are available (see Table 1). Other objects, however, show completely featureless spectra, as in the case of Asbolus. *Romon-Martin et al.* (2002) reported detailed near-infrared observations for Asbolus over the complete rotational period with high signal precision and they did not detect any features or any variability with rotation. They model the surface composition with a mixture of Triton and Titan tholins, ice tholin, and amorphous carbon. For some objects, even when observed with large telescopes, the measured spectra are incomplete or of fairly low quality.

With a small number of exceptions described below, all the spectra are either featureless to the level of the noise or show varying levels of the 1.5- and 2.0-μm absorptions due to water ice. *Barkume et al.* (2007) quantify the water-ice absorption depth and classify each of the spectra by a simple proxy for the amount of water-ice absorption. They define A_w as the fractional difference between the reflectance at 1.7 μm, in the water ice continuum, and at 2.0 μm, in the middle of the water-ice absorption band. This proxy, along with its associated error, gives a good indication of not only the shape of the spectrum, but also the quality. Barkume et al. (in preparation) found that 65% of their observed TNOs show no definitive absorptions due to water ice. Some objects with poorer signal precision, like 1996 TP_{66} (Fig. 2), may have small signatures. A plot of visible spectral gradient vs. water-ice absorption depth is shown in Fig. 4. *Brown et al.* (2007) identified a cluster of objects with absorption depths greater than 43% associated with a collisional family, whereas the remaining TNOs have water absorption depth less than 25% or no absorption. No correlation between the presence/amount of water-ice absorption and slope gradient appears when the hypothesized dynamical family has been removed.

Only a small number of objects show near-infrared absorption features attributable to any species other than water ice. Most prominently, the largest TNOs — Eris, Pluto, and 2005 FY_9 — each have complex spectra dominated by absorption bands due to methane (see chapter by Brown). The Centaur Pholus shows strong absorption bands at 2.04 and at 2.27 μm. *Cruikshank et al.* (1998) modeled the complete spectrum of Pholus from 0.4 to 2.5 μm interpreting the surface composition with the presence of the silicate olivine, Titan tholins, water ice, methanol, and carbon. They suggested that Pholus could be a primitive object, a large comet nucleus that has never been active. Two TNOs also show the 2.27-μm absorption, which has been interpreted as methanol. 55638 2002 VE_{95} was observed at VLT-ESO by *Barucci et al.* (2006) in the visible and near-infrared. The spectra show clear absorption at 1.5, 2.0, and 2.27 μm, implying the presence of H_2O and CH_3OH (and/or a photolytic product of methanol). The spectrum is similar to that of Pholus, though 2002 VE_{95} is less red. 1996 GQ_{21} also has a spectrum similar to that of Pholus (*Brown,* 2003; Barkume et al., in preparation). These detections are potentially important, suggesting a chemically primitive surface, since heating and other processes remove the light hydrocarbons in favor of macromolecular carbon.

3.4. Far Infrared: Spitzer Space Telescope Observations

As a technique for characterization of solid surfaces, thermal emission spectroscopy has been somewhat underexplored, not only for TNOs and Centaurs, but for minor bodies as a whole. The main reason is that strong absorption bands and rapid variability in Earth's atmosphere make such observations very difficult from the ground, even for the brightest asteroids. The ISO satellite demonstrated the utility of this technique for small bodies, detecting spectral emissivity features on several bright asteroids, particularly several belonging to primitive taxonomic classes (*Barucci et al.,* 2002c; *Dotto et al.,* 2002, 2004). Spitzer's significantly higher sensitivity as compared to ISO and groundbased observations opens the door for thermal emission spectroscopy of TNOs and Centaurs.

The mid-IR (5–38 μm) is well-suited to investigating the composition and structure of the surfaces of these objects. This spectral region contains the Si-O stretch and bend fundamental molecular vibration bands (typically in the ranges 9–12 and 14–25 μm, respectively). Interplay between surface and volume scattering around these bands creates complex patterns of emissivity highs and lows that are very

TABLE 1. Diameter (in kilometers), ices observed, taxonomic group (*Barucci et al.,* 2005b), and dynamical group (C: Centaurs, Cl: classical, R: resonant, S: scattered, and D: detached objects), as defined in the chapter by Gladman et al., of the TNOs and Centaurs available in the literature.

Object	Ices (Ref)	Diameter (Ref)	Tax. G	Dyn. G.	H_2O depth
2060 Chiron (1977 UB)	H_2O, var. (Lu00, Fo99, Ro03)	150 ± 10 (Fe02)	BB	C	—
5145 Pholus (1992 AD)	H_2O, CH_3OH (Cr98)	155 ± 44 (St)	RR	C	12 ± 3
8405 Asbolus (1995 GO)	none (Ke00*, Ba00, Br00a, Ro02)	85 ± 12 (Fe02, St)	BR	C	—
10199 Chariklo (1997 CU_{26})	H_2O (BrK98, Dot03c)	262 ± 18 (St)	BR	C	11 ± 3
31824 Elatus (1999 UG_5)	H_2O, var. (Bau02)	48 ± 14 (St)	RR	C	—
32532 Thereus (2001 PT_{13})	H_2O, var. (Ba02a, Me05, Li05)	61 ± 13 (St)	BR	C	—
52872 Okyrhoe (1998 SG_{35})	H_2O? (Dot03a)	52 ± 10 (St)	BR	C§	—
55576 Amycus (2002 GB_{10})	H_2O? (Dor05)	77 ± 12(St)	RR	C	—
63252 (2001 BL_{41})	none (Dor03)	20‡	BR	C	—
83982 Crantor (2002 GO_9)	H_2O (Dor05)	67 ± 19 (St)	RR	C	—
15789 (1993 SC)	none (Je01)	330 ± 66 (Th00)	RR	R	0 ± 10
15874 (1996 TL_{66})	none (Lu98)	630 ± 90 (Th00)	BB	S	0 ± 8
15875 (1996 TP_{66})	none (Bark07)	171 ± 49 (St)	RR	R	–1 ± 11
19308 (1996 TO_{66})	H_2O, var. (Br99)	<900 (Al04)	BB	Cl	65 ± 5
19521 Chaos (1998 WH_{24})	none (Bark07)	450‡	IR	Cl	–6 ± 4
20000 Varuna (2000 WR_{106})	H_2O? (Li01), (Bark07)	624 (–140, +179) (St)	IR	Cl	6 ± 3
24835 (1995 SM_{55})	H_2O (Bark07)	140‡	BB	Cl	43 ± 13
26181 (1996 GQ_{21})	none (Dor03) H_20,CH_3OH (Bark07)	400‡	RR	R	9 ± 3
26375 (1999 DE_9)	H_2O (Je01, Bark07)	461 ± 45 (St)	IR	R	18 ± 5
28978 Ixion (2001 KX_{76})	H_2O? (Li02, Boe04, Bark07)	574 ± 140 (St)	IR/RR	R	9 ± 4
29981 (1999 TD_{10})	H_2O (Bark07)	104 ± 13(St)	BR	S	13 ± 4
38628 Huya (2000 EB_{173})	H_2O? (Br00b, Je01, dB04)	540±40 (St)	IR	R	6 ± 3
42301 (2001 UR_{163})	none (Bark07)	620‡	RR	R	–7 ± 10
47171 (1999 TC_{36})	H_2O (Dot03a, Me05)	414 ± 38(St)	RR	R	14 ± 4
47932 (2000 GN_{171})	none (dB04, Bark07	400 (Sh02), 322 ± 54 (St)	IR	R	–8 ± 6
50000 Quaoar (2002 LM_{60})	H_2O (Je04)	1280 ± 190 (Br04)	RR?	Cl	20 ± 1
54598 Bienor (2000 QC_{243})	H_2O (Dot03a)	206 ± 30 (St)	BR	S	—
55565 (2002 AW_{197})	H_2O (Dor05), none (Bark07)	700±50 (Cr05)	IR	Cl	0 ± 3
55636 (2002 TX_{300})	H_2O (Li006b, Bark07)	643±210	BB	Cl	65 ±4
55637 (2002 UX_{25})	none (Bark07)	682 ± 114	IR	Cl	3 ± 3
55638 (2002 VE_{95})	H_2O, CH_3OH (Bar06)	400‡	RR	R	20 ± 4
65489 Ceto (2003 FX_{128})	H_2O (Bark07)	229 ± 18	—	D	14 ± 11
66652 (1999 RZ_{253})	none (Bark07)	280‡	RR	Cl	–13 ± 13
79360 (1997 CS_{29})	none (Gr05)	400‡	RR	Cl	0 ± 10
84522 (2002 TC_{302})	none (Bark07)	1149 ± 325	—	S	–1 ± 7
84922 (2003 VS_2)	H_2O? (Bark07)	729 ± 188(St)	—	R	7 ± 2
90377 Sedna (2003 VB_{12})	CH_4, N_2 (Ba05a, Tr05†)	2000‡	RR	D	—
90482 Orcus (2004 DW)	H_2O (Fo04a, dB05, Tr05)	951±74 (St)	BB	R	22 ± 4
119951 (2002 KX_{14})	none (Bark07)	565 ± 182	—	C	1 ± 17
120178 (2003 OP_{32})	H_2O (Bark07)	850‡	BB?	Cl	77 ± 4
134340 Pluto	CH_4, CO, N_2 (Ow93)	2350 ± 60 (Mi93, Th89)	BR	R	—
136108 (2003 EL_{61})	H_2O (Tr07)	2000 ± 500 (Ra) 1342±133 (St)	BB	Cl	55 ± 1
136199 Eris (2003 UB_{313})	CH_4, N_2? (Br05, Mer06)	3000±300 (Be06) 2450 ± (Br06)	BB	D	—
136472(2005 FY_9)	CH_4 (Li06a)	1905 ± 100 (St)	BR	Cl	—

TABLE 1. (continued).

Object	Ices (Ref)	Diameter (Ref)	Tax. G	Dyn. G.	H_2O depth
2003 AZ_{84}	H_2O (Bark07)	688 ± 99(St)	BB	Cl	22 ± 7
2005 RN_{43}	none (Bark07)	220‡	—		0±3
2005 RR_{43}	H_2O (Bark07)	200‡	—		60±7
Charon	HO_2O, NH_3 (Br00c)	1208 ± 15 (Si06, Gu06)	BB?	~	58 ± 3
S/2005 (2003 EL_{61}) 1	H_2O (Bark06)		BB?		87 ± 11

**Kern et al.* (2000) claimed to have detected water ice on one side, but the results have been contradicted by later observations.
†*Trujillo et al.* (2005) obtained a largely featureless spectrum.
‡If we assume an albedo of 0.10.
§Now classified as JFC (see chapter by Gladman et al.).

In the last column the H_2O depth has been reported as computed by Barkume et al. (in preparation); var = reported for objects whose spectra show variation in ice content.

References: Al04 = *Altenhoff et al.* (2004); Ba00 = *Barucci et al.* (2000); Ba02 = *Barucci et al.* (2002a); Ba05a = *Barucci et al.* (2005a); Br06 = *Brown et al.* (2006); Bark06 = *Barkume et al.* (2006); Bark07 = Barkume et al. (in preparation); Bau02 = *Bauer et al.* (2002); Be06 = *Bertoldi et al.* (2006); Boe04 = *Boehnhardt et al.* (2004); Br99 = *Brown et al.* (1999); Br00a = *Brown* (2000); Br00b = *Brown et al.* (2000); Br00c = *Brown and Calvin* (2000); Br04 = *Brown and Trujillo* (2004); Br05 = *Brown et al.* (2005); BrK98 = *Brown and Koresko* (1998); Bark = *Barkume et al.* (2006); Cr98 = *Cruikshank et al.* (1998); Cr05 = *Cruikshank et al.* (2005); dB04 = *de Bergh et al.* (2004); dB05 = *de Bergh et al.* (2005); Dor03 = *Doressoundiram et al.* (2003); Dor05 = *Doressoundiram et al.* (2005); Dot03a = *Dotto et al.* (2003a); Dot03c = *Dotto et al.* (2003b); Fe02 = *Fernandez et al.* (2002); Fo04a = *Fornasier et al.* (2004a); Fo99 = *Foster et al.* (1999); Gr96 = *Grundy and Fink* (1996); Gr05 = *Grundy et al.* (2005); Gu06 = *Gulbis et al.* (2006); Je01 = *Jewitt and Luu* (2001); Je04 = *Jewitt and Luu* (2004); Ke00 = *Kern et al.* (2000); Li01 = *Licandro et al.* (2001); Li02 = *Licandro et al.* (2002); Li05 = *Licandro and Pinilla-Alonso* (2005); Li06a = *Licandro et al.* (2006a); Li06b = *Licandro et al.* (2006b); Lu98 = *Luu and Jewitt* (1998); Lu00 = *Luu et al.* (2000); Me05 = *Merlin et al.* (2005); Mi93 = *Millis et al.* (1993); Ow93 = *Owen et al.* (1993); Ra = *Rabinowitz et al.* (2006); Ro02 = *Romon-Martin et al.* (2002); Ro03 = *Romon et al.* (2003; Sh02 = *Sheppard and Jewitt* (2002; Si06 = *Sicardy et al.* (2006; St = chapter by Stansberry et al.; Th89 = *Tholen and Buie* (1989); Th00 = *Thomas et al.* (2000); Tr05 = *Trujillo et al.* (2005); Tr07 = *Trujillo et al.* (2007).

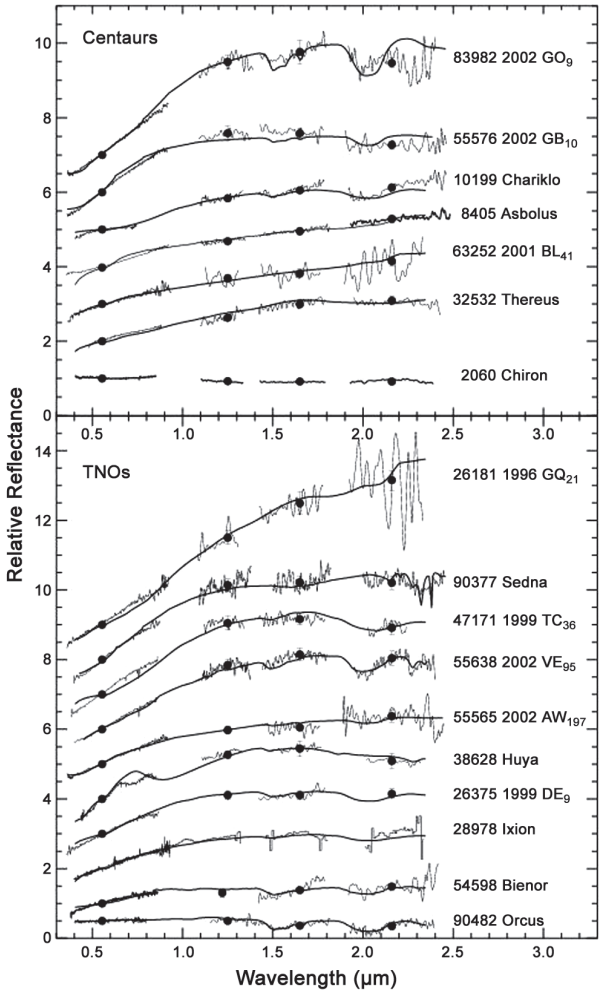

sensitive to, and therefore diagnostic of, silicate mineralogy (e.g., *Salisbury et al.,* 1992; *Hapke,* 1996; *Witteborn and Roush,* 2000; *Cooper et al.,* 2002). Relevant ices (e.g., H_2O, CH_3OH) also exhibit features in this wavelength range. These bands, particularly the Si-O fundamentals, are also very sensitive to grain size and surface structure.

The Infrared Spectrograph (IRS) (*Houck et al.,* 2004) measures the thermally emitted flux density (e.g., units of Jy) as a function of wavelength of TNOs and Centaurs. In this thermal flux spectrum, the compositionally diagnostic emissivity features are superposed on the thermal continuum. The thermal continuum depends on many factors, including the object's size, albedo, thermal inertia, distance from the Sun, and surface roughness. Emissivity spectra are derived by dividing the measured flux spectrum by a model of the thermal continuum. Allowing the radius and albedo to vary in the model in order to find the best thermal continuum fit to the SED results in estimates of these parameters. This is the same method as described for the MIPS radiometry in the chapter by Stansberry et al., but with a different dataset. The absolute calibration of IRS has an uncertainty of ~10%, which propagates to uncertainties of ~5% in the size estimate (see *Emery et al.,* 2006, for further discussion).

Fig. 3. Visible and near-infrared spectra with broadband photometric points at V, J, H, and K of some Centaurs and TNOs observed at VLT (ESO). The continuous lines superimposed on the spectra are the best-fit spectral models (see Table 1 for references). The spectra are normalized at 0.55 μm. Spectra are shifted by one unit for clarity.

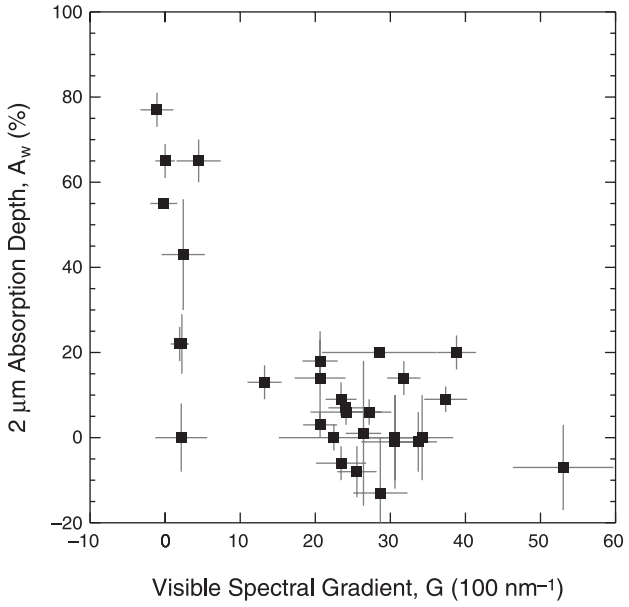

Fig. 4. The 2-μm absorption depth vs. visible color gradient for all TNOs (see Table 1) with available near-infrared spectra and colors. The cluster of objects with no spectral gradient and high water ice absorption are all associated with the 2003 EL_{61} collisional family (*Brown et al.,* 2007).

The large heliocentric distances (and therefore cold surfaces) of TNOs and Centaurs preclude observations over the full range of IRS. Current Spitzer/IRS programs include two Centaurs that are observed from 7.5 to 38 μm, four Centaurs that cover 14.2–38 μm, and 11 TNOs and Centaurs only in the longest wavelength module (20–38 μm). Five of these objects were not detected, presumably because their albedos are higher than expected and therefore their thermal fluxes were lower than expected. Initial results in terms of surface characteristics are summarized below.

The Centaur 8405 Asbolus was bright enough to be observed from 7.5–38 μm (Fig. 4). The emissivity spectrum of Asbolus exhibits emission bands with strong spectral contrast, similar to those of three Trojan asteroids (see chapter by Dotto et al.). An emissivity high is evident near 10 μm. This is presumably a plateau like in the Trojan spectra, although the Asbolus spectrum cuts off on the short wavelength side before the emissivity comes back down. There is also a broad rise from about 18 to 28 μm with an apparent double peak near 19 and 24 μm. The strong emissivity plateau near 10 μm and the broader emissivity high near 20–25 μm are interpreted as fine-grained silicates. Large grain sizes behave very differently, with emissivity lows at these locations (e.g., *Christensen et al.,* 2000). However, the emissivity bands measured by IRS in Asbolus (and the Trojans) also do not exactly match those expected for regolith surfaces; the 10-μm plateau is narrower and the spectra do not rise as rapidly near 15 μm. Analysis of these differences is in progress. Surface structure is very likely playing an important role. In particular, having fine-grained silicate particles embedded in a matrix that is fairly transparent at these wavelengths (e.g., macromolecular organic solids) may help resolve some of these differences (*Emery et al.,* 2006).

The V-NIR reflectance spectrum (0.3–2.5 μm) of Asbolus is moderately red with no detectable absorption features. The V-NIR colors place it in the BR spectral class (see chapter by Fulchignoni et al.), and the albedo is very low. These characteristics are also very similar to Trojan asteroids and are consistent with silicate surface compositions (*Cruikshank et al.,* 2001; *Emery and Brown,* 2004).

Most of the other Centaurs and TNOs observed with IRS are much fainter than Asbolus and the Trojans, and consequently the emissivity spectra obtained for them are somewhat poorer in quality (lower signal precision). Spectra of four objects are shown along with Hektor and Asbolus in Fig. 5. These have been binned to lower spectral resolution to improve the signal precision. The emissivity spectrum of Elatus is similar to that of Asbolus, with a broad high from ~17 to 27 μm, although possible double peaks are at slightly different wavelengths. *Bauer et al.* (2002) report

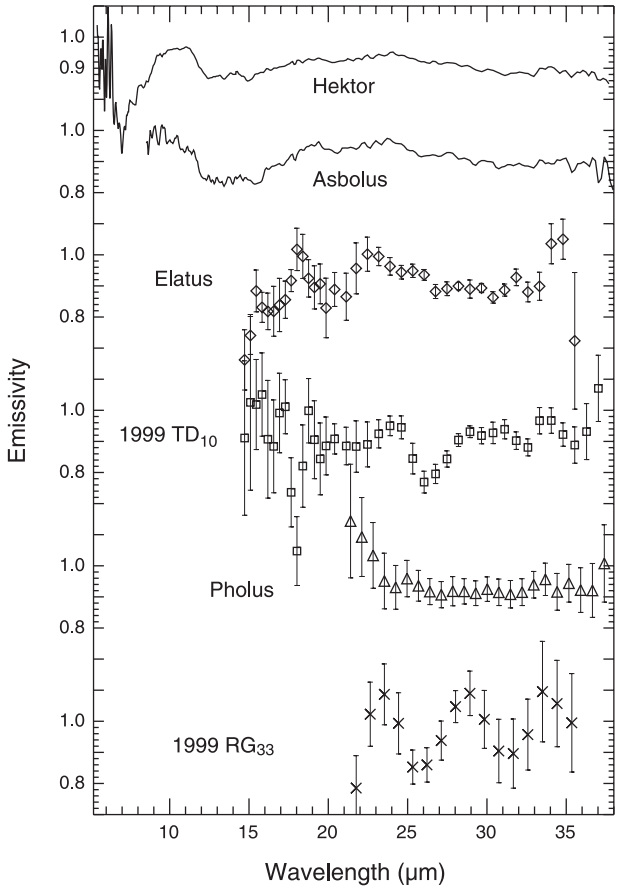

Fig. 5. Emissivity of several objects from the Spitzer Space Telescope. The spectra of 31824 Elatus (diamonds), 29981 1999 TD_{10} (squares), and 5145 Pholus (triangles) are Gaussian binned with a FWHM of eight spectral channels, and the spectrum of 15504 1999 RG_{33} (× symbols) is similarly binned with a FWHM of 10 channels. 624 Hektor is a Trojan asteroid, shown for comparison.

rotational variation in the spectrum of Elatus, which varies in spectral class from BR and featureless to IR with H_2O-ice bands. The BR and featureless spectrum is consistent with the similarity of the emissivity spectrum to that of Asbolus. The emissivity spectra of 1999 TD_{10} and 1999 RG_{33} both contain an emissivity low near 26 μm. The origin of this feature is uncertain at this point, but may be diagnostic of silicate mineralogy or ices on the surface (although it does not seem to match any known H_2O bands). It is interesting to note that although both of these objects are in highly eccentric orbits (0.77 and 0.87 for RG_{33} and TD_{10}, respectively), their perihelion distances are significantly different (2.16 and 12.28 AU). No near-infrared spectrum has been published for either of these two objects. The emissivity spectrum of Pholus displays no diagnostic bands, despite having a very active near-infrared reflectance spectrum.

4. INTERPRETATION AND SPECTRAL MODELING

4.1. Scattering Theories

Several methods have been developed to calculate synthetic reflectance spectra for comparison with the observational data for planetary surfaces. The goal of such modeling is to constrain grain sizes and mixing characteristics of the various ices, minerals, and organic materials from which those surfaces are composed. Slightly different approximations of radiative transfer theory are used to analyze the diffuse scattering of light from the surface of a semi-infinite particulate medium.

The radiative transfer model is well established for light scattering from dispersed particulate media (*Chandrasekhar,* 1960). However, *Hapke* (1981) was one of the first to formulate a theory of light scattering for surfaces in which the particles are close together. The methods described here, those of *Hapke* (1981) and *Shkuratov et al.* (1999), use the radiative transfer equation within a small elementary volume of the scattering medium, which is characterized by the albedo of single scattering. Both formulations are derived in the geometrical-optics approximation.

4.1.1. Hapke theory. The "bidirectional reflectance theory" of Hapke is based on the equations of radiative transfer for an optically thick, plane-parallel particulate medium. These equations are relatively simple, and can be used even though real planetary surfaces are extremely complex because we do not (and cannot) know many of the physical parameters that would enter into a more complex theory. This simplification permits a fast and accurate numerical evaluation. Moreover, the differences between the approximations of of the Hapke theory (*Hapke,* 1981) and the exact solution of Chandrasekhar are small, especially for low-albedo bodies, which is usually the case in the TNO population (see section 3.3). Because of its simplicity and accuracy, this theory has become the most widely used in the planetary community. We explain it, briefly, in this section.

The bidirectional reflectance of a medium is defined as the ratio of the scattered radiance at the detector to the incident irradiance. The reflectance $r(\mu_0, \mu, g)$ of a surface consisting of particles of arbitrary shape in close proximity depends on incident light angle i ($\mu_0 = \cos i$), emergent light angle e ($\mu = \cos e$), and phase angle (g), and can be computed by

$$r(\mu_0, \mu, g) = \frac{w\mu_0}{4\pi\mu_0 + \mu}[(1 + B(g))P(g) + H(\mu_0)H(\mu) - 1] \quad (1)$$

Equation (1) considers single-scattering with w, the single-scattering albedo, and multiple-scattering with $H(\mu)$ and $H(\mu_0)$, the multiple-scattering functions. P(g) is the phase function due to the singly scattered radiation, which can be isotropic or not, and B(g) describes the opposition effect.

The average single-scattering albedo w is the ratio of the average scattering coefficient of the medium to the average extinction coefficient of the medium and can be expressed as

$$w = S_e + (1 - S_e)\frac{1 - S_i}{1 - S_i\Theta}\Theta \quad (2)$$

This equation (2) depends on the external (S_e) and internal (S_i) surface-scattering coefficients and the absorption coefficient (Θ), which are related to the microscopic quantities n, k (the real and imaginary part of the complex index of refraction respectively), and D (the average diameter). The absorption coefficient, for a given wavelength (λ), is equal to

$$\Theta = e^{\frac{2\alpha D}{3}} \text{ with } \alpha = \frac{4\pi nk}{\lambda}$$

The two multiple-scattering functions are approximated by the same following form

$$H(\mu) = \frac{1 + 2\mu}{1 + 2\mu\sqrt{(1 - w)}} \text{ and } H(\mu_0) = \frac{1 + 2\mu_0}{1 + 2\mu_0\sqrt{(1 - w)}}$$

for low, fixed w, we note that $H(\mu)$ or $H(\mu_0)$ show little variations. A simple approximation for the phase function of nonisotropic scatters is a first-order Legendre polynomial

$$P(g) = 1 + b\cos(g) \quad (2a)$$

In the case of isotropic scattering, P(g) = 1 and in the cases of highly anisotropic scatterers, P(g) = 1 + cos(g) or 1 – cos(g) for backscattering or forward-scattering, respectively. An alternative expression that is sometimes used for the phase function is a Henyey-Greenstein function (1941), which depends on the asymmetry parameter ξ

$$P(g) = \frac{(1 - \xi^2)}{(1 - 2\xi\cos(g) + \xi^2)^{3/2}} \quad (2b)$$

This parameter determines whether the particle is backscattering ($\xi < 0$) or forward-scattering ($\xi > 0$). The first-order expansion (equation (2b)) is adequate if the phase function is single-lobed, but limited in the case of real phase function. Nevertheless, the Henyey-Greenstein function allows the description of a wide range of phase functions and can be used with a high level of confidence.

The opposition effect refers to the tendency of surface reflectance to increase dramatically at very small phase angles. An approximation of the theory of shadow-hiding in a medium, revisited by *Hapke* (1986), is

$$B(g) = \frac{B_0}{1 + \tan(g/2)/h} \quad (3)$$

In equation (3), B(g) describes completely the opposition effect. B_0, an empirical factor comprised between 0 and 1, is the ratio of the near-surface contribution to the total particle scattering at zero phase angle (*Hapke,* 1986). When the particles are opaque then all the scattered light comes from the surface of the particle: B_0 maximizes and becomes equal to 1. The backscatter parameter h depends on the surface properties [it is essentially equal to the ratio of the mean size of the openings between soil particles $\langle a_e \rangle$ to the extinction mean free path (1/E)]

$$h = \frac{E}{2}\langle a_e \rangle$$

Typical values of h are close to 0.4 for uncompacted lunar soil (*Hapke,* 1966) and ~0.1–0.2 for cobalt glass powders (*Hapke and Wells,* 1981).

Several subsequent improvements take into account rough surfaces (*Hapke,* 1984). For TNO observations, which involve low phase angles and relatively low albedos, the correction factors appear to be negligible. We note that the model is reasonably well understood and available for scattering and emission of radiation from regoliths with grain sizes that are large compared to the wavelength. *Hapke et al.* (1997) gives a formula, based on laboratory studies, for grain sizes on the order of the wavelength in the aim of completing his theory for a plane-parallel particulate medium.

Equation (1) can be used to compute the bidirectional reflectance of a medium composed of spheroidal, closely packed particles of a single component. To relate reflectance TNO spectra to synthetic spectra of a mixture of compounds, we have two choices. The first one is to assume an areal mixture. All reflectances of independent components i are linearly combined to represent the total reflectance r_T of the multicomponent surface

$$r_T = \sum_{i=1}^{N} c_i r_i$$

where c_i is the surface proportion of each component of bidirectional reflectance r_i.

On the other hand, we can assume a homogeneous mixture (intimate). The bidirectional reflectance is governed by w_T and if the particles are greater than the wavelength and are close together, w in equation (1) becomes w_T

$$w_T = \frac{\sum_{i=1}^{N} \frac{M_i}{\rho_i D_i} w_i}{\sum_{i=1}^{N} \frac{M_i}{\rho_i D_i}}$$

where w_T is the mean single-scattering albedo of all the particles, M_i is the bulk density of type i particles with solid density ρ_i, single-scattering albedo w_i, and diameter D_i.

4.1.2. Shkuratov method. In the model by *Shkuratov et al.* (1999), multiple reflections in a particle are considered as multiple-scattering in a one-dimensional medium with the same effective reflection coefficients. This approach replaces scattering in a system of particles by scattering in an equivalent system of plates, with the assumption that the calculated one-dimensional reflectance is equal to the reflectance of a three-dimensional medium at small phase angles.

At the boundary of the medium, light propagation is a random branching process and each ray is characterized by its reflection and transmission (R and T respectively), which depend on the complex refractive index n and k (optical constants) of the material and on the local angle of incidence on the particle interface. Transmission and reflection take place when the ray of light enter or leave the particle (see Fig. 6), inducing several types of transmission, and reflection (T_e, T_i, $T_{i'\ldots}$) and (R_e, R_i) respectively.

For a homogeneous particle, there are simple relations between transmissions and reflections. We note that $T_e = 1 - R_e$ and $T_i = 1 - R_i$ and each term is computed using empirical approximations and the usual Fresnel coefficients (r_0)

$$r_0 = \frac{(n-1)^2}{(n+1)^2},\ R_e \approx r_0 + 0.05,\ R_b \approx (0.28 \cdot n - 0.20)R_e$$

$$R_i \approx 1.04 - 1/n^2, \text{ and } R_f = R_e - R_b$$

where R_b and R_f are the average backward and forward reflectance coefficients, respectively.

In this model, the single-scattering albedo of a particle is the sum of the fractions of the fluxes scattered by a particle into the backward (r_b) and forward (r_f) hemispheres (see equations (4a) and (4b)) and depends on the optical density between the branching ($\tau = 4\pi kD/\lambda$). The values (r_b) and (r_f) represent an evaluation of the probabilities of the beam emerging backward or forward at a given scattering number (see *Shkuratov et al.,* 1999, for more details about the evaluation of each of the probabilities of T_i, $T_{i'}$, etc.).

$$r_0 = R_b + \frac{T_e T_i R_i e^{(-2\tau)}}{2(1 - R_i e^{(-\tau)})} \quad (4a)$$

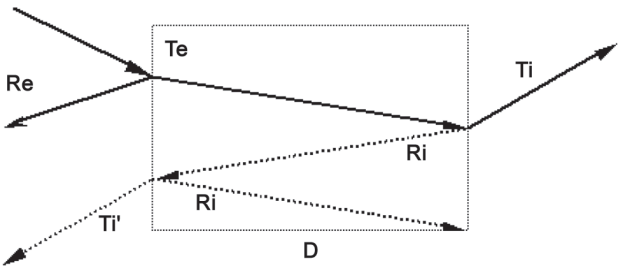

Fig. 6. Schematic diagram of the light propagation in a medium of length D used in the Shkuratov method.

$$r_f = R_f + T_e T_i e^{(-\tau)} \frac{T_e T_i R_i e^{(-2\tau)}}{2(1 - R_i e^{(-\tau)})} \qquad (4b)$$

Up to this point, the theories of Hapke and Shkuratov are relatively similar in terms of computing the single-scattering albedo of a homogeneous medium. More significant differences arise in the computation of the reflectance of a particulate surface. Indeed, contrary to Hapke's model, the Shkuratov model takes into account the porosity p of the medium. The reflectance r is given by

$$r = \frac{1 + \beta? - \varphi?}{2\beta} - \sqrt{\left(\frac{1 + \beta? - \varphi?}{2\beta}\right)^2 - 1} \qquad (5)$$

where $\beta = (1 - p)r_b$ and $\varphi = (1 - p)r_f + p$.

Moreover, the phase function asymmetry is not a free parameter but a dependent variable that is determined by the grain radius and the composition (see *Poulet et al.,* 2002). Similar to Hapke theory, the different mixtures of ices and mineral can be areal mixtures, or intimate mixtures with or without fine absorbing and independent inclusions. In the case of no inclusions, the relations to compute the reflectance (equation (5)) of a surface composed of several components of concentration c_i are

$$\beta = (1 - p)\sum_i (c_i \cdot r_{bi}) \text{ and } \varphi = (1 - p)\sum_i (c_i \cdot r_{fi}) + p$$

The ability to incorporate inclusions allows us to use components with a particle size that is very small compared to the wavelength λ in the bulk or near the surfaces of coarse particles. These inclusions, which are very small, are approximated to be spherical. Mie theory is applied, and the contribution of absorbing inclusions to the imaginary part of refractive index, k, which can be represented as changed as $k = k + k_a$, were

$$k_a = 3/2c \cdot n \cdot \mathrm{Im}\frac{\varepsilon - 1}{\varepsilon + 2}$$

In this equation, c is the volume concentration of the inclusion in the matrix and e the ratio of the complex dielectric constant of the inclusion to that of the matrix. Note that n is the real part of the matrix refractive index. The dielectric function is related to optical constants through the constitutive relations

$$\varepsilon = \varepsilon' + i\varepsilon'' \text{ with } \varepsilon' = n^2 + k^2 \text{ and } \varepsilon'' = 2nk$$

When the inclusions are formed by space weathering (e.g., solar wind, heating by impact processes, or high-energy flux from the interstellar medium), fine inclusions frequently occur near the surface in a layer of a thickness $d \ll \lambda$. If such inclusions are present on particles, the light beam passes the absorbing layer twice per each scattering, increasing the optical density. For $c \ll 1$ the Mie theory can again be applied, and k becomes

$$k = k + \frac{2d}{2D}k_a$$

One of the most significant differences between the models of Hapke and Shkuratov is the treatment of scattering asymmetry. In the Hapke model, the particle phase function itself is an input parameter to the model (a first-order Legendre polynomial scattering function or a Henyey-Greenstein function), as is the asymmetry parameter, for whichever phase function is used. Recall that the asymmetry parameter describes the relative importance of back- or forward-scattering. In the Shkuratov model, on the other hand, the particle phase function asymmetry is directly determined by the grain size and the composition, and can be characterized by the ratio rf – rb/rf + rb. Scattering asymmetry affects the dark and bright parts of a given spectrum in a nonproportional manner (*Poulet et al.,* 2002). Other small differences are that Shkuratov specifically includes porosity (although it is possible to approximate porosity effects in to Hapke model in an *ad hoc* manner) and the fact that observational geometry is not mentioned in the Shkuratov model, contrary to that of Hapke.

Finally, we mention the radiative transfer model of *Doute and Schmitt* (1998), developed for the calculation of bidirectional reflectance by a parallel plane that is absorbing, scattering, and slightly stratified. This model follows the approach of Hapke but improves the realism of the single- and double-scattering contribution with an unrestricted phase function; the form of the phase function equation (2a) is only used for the higher-order scattering. Concerning stratification, a simple adding algorithm based on the principle of invariance is used (*Doute and Schmitt,* 1998), which improves the results more (e.g., *Doute et al.,* 1999, for Pluto) compared to areal and intimate models. This model allows the analysis of hyperspectral images, even if this aspect is not useful for groundbased observations.

4.2. Limits and Dependences

Although these models are generally able to describe the spectral properties of the analyzed objects quite well, it is important to note that they are only indicative. Mixtures with different grain sizes or different mixing ratios of the constituents can give very similar fits to the data. Therefore, an absolute determination of the surface composition is difficult. Moreover, many of the parameters are not well established or completely unknown. Limits and dependences about the models' parameters are presented below.

4.2.1. Grain size and concentration. The grain size and the abundance of particles directly affect the optical depth of the light. The presence and strength of absorption bands can inform us not only of the terrain composition, but also of its texture. In the Hapke or Shkuratov models, the con-

centration and grain size are generally linked, particularly for ices, and the determination of both values is difficult. Very similar model spectra can often be obtained with larger grain size and weak concentration or small grain size and large concentration. However, very deep absorption bands usually imply a large grain size and imply that the terrain texture is a compact solid surface rather than a granular surface, especially when the models require centimeter-sized grains. Both models require grains with a diameter several times larger than the wavelength — the entire development of Hapke or Shkuratov models are based on this assumption — and the use of smaller grain sizes violates the principle of geometrical optics. Nevertheless, *Piateck et al.* (2003) has shown by laboratory experiments that the scattering properties of small particles, for reasons not yet understood, disagree strongly with predictions that assume the particles scatter independently, and work is still in progress to understand the detailed scattering properties of very small particles.

4.2.2. Compounds and optical constants. Optical constants are the basis of the intimate mixture modeling. Each optical constant is derived from laboratory measurements for a given molecule. These molecules can be pure or sometimes diluted. Optical constants are most often derived from measured transmittance using the Kramers-Kronig relation. The reflectance of a medium measured in the laboratory is relevant only for the particle size of the given experiment, while optical constants allow the generation of model spectra for different particle sizes and the reproduction of not only geographical mixtures but also intimate mixtures. Optical constants also depend on the properties of the particles, such as the state of the molecules or the degree of crystallization at a given temperature. Obviously, it is essential to have a complete set of optical constants, including a variety of components (ices, organic compounds, minerals, carbons, etc.) at several temperatures (see chapter by de Bergh et al.).

4.2.3. Temperature and dilution. The temperature and dilution of molecules in a matrix are important factors, the variation of which can induce spectral variations (e.g., wavelength shifts and band depths). For example, in the case of crystalline water ice, the absorption bands are deeper at lower temperatures (e.g., the 1.31 and 1.65 ìm bands) (*Grundy and Schmitt,* 1998) and also show slight shifts in wavelength. For methane ice diluted in a nitrogen ice medium, the wavelength shift of the methane absorption bands are directly related to the concentration of this ice (*Quirico and Schmitt,* 1999). We note that the pure or diluted state of certain molecules can be observed spectroscopically. For example, not only do the wavelengths of the methane bands shift in dilution, but the 1.69-μm band appears only when methane is pure. Once again, the need to have a large variety of optical constant of numerous molecules at different temperatures and dilution states is mandatory.

4.2.4. Asymmetry parameter. The asymmetry factor is often unknown and its assumed value is based on comparison with other small bodies of the solar system located more or less in the same region. For icy satellites, this value is determined using photometric parameters computed by fitting the Hapke model to remote sensing data. However, the backscattering behavior generally used on icy satellites (corresponding to a negative asymmetry factor) may be a bias introduced by the Hapke model. Indeed, for sparsely distributed, independently scattering grains, the calculated asymmetry parameters are always positive or may be negative only in few cases for densely packed grains (*Mishchenko,* 1994). The under- or overestimation of this factor increases or decreases the entire reflectance in the same way and induces little variations of compound concentration or particle size in the models.

4.2.5. Albedo. The albedo is a measure of the light reflected by the body, and while in the strictest quantitative sense the albedo is dependent on geometric and other factors, here we refer simply to the ratio of reflected light to the incident sunlight, and express this quantity in percent. The knowledge of this value is fundamental to constraining the concentration of ices, carbons, and organics, which can have widely differing reflectivities. For bright bodies, like Pluto or Eris, the high albedo, close to 60–86%, indicates the presence of a large quantity of ices on the surface. This is contrary to dark objects, for which the albedo can be <5%, indicating the presence of dark carbons or organics on the surface.

4.3. Surface Modeling Application

The use of a radiative transfer model is the most realistic and reliable way to interpret the observed spectra and to investigate the surface composition of planetary objects. For an appropriate application of the method, a complete spectrum from the visible and near-infrared is necessary, as is the albedo. In cases where different spectral segments were obtained separately, photometric data are also needed to properly adjust these segments relative to one another.

To illustrate the application of the models described above, we give here an example of the investigation of the surface composition of the Plutino 55638 (2002 VE_{95}), considering areal and intimate mixtures of different materials. Several minerals, ices, and different organic complexes (e.g., tholins and kerogens) at different grain sizes have been considered. The best-fit model is obtained by varying the critical parameters — composition, abundance, and grain size — until the difference between the data and the model spectrum is minimized. In this case, the Levenberg-Marquard minimization algorithm (*Press et al.,* 1986) was used. The albedo of 2002 VE_{95} is unknown, and we assume it equals 0.10 at 0.55 μm, a mean value for TNOs (see chapter by Stansberry et al.). Intimate mixtures give the better matches (as measured by χ^2) than areal mixtures over the spectral range between 0.4 and 2.4 μm. The synthetic spectra obtained with the two models (Hapke and Shkuratov) represent similar quality fits of the spectrum and give similar results but with different percentages of components (Fig. 7).

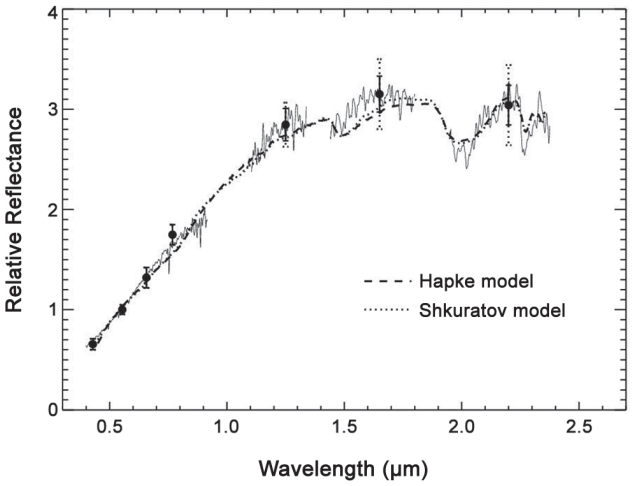

Fig. 7. Spectral reflectances of 55638 (2002 VE_{95}) obtained in V, J, H, and K bands (full lines) and adjusted using photometric colors, which are represented by dots with the relative errors (*Barucci et al.,* 2006). The two best-fit intimate models have also been reported.

The best-fit Hapke model is composed of 12% amorphous H_2O ice (with grain size of 30 μm), 10% CH_3OH ice (40 μm), 47% Titan tholin (4 μm), 14% Triton tholin (4 μm), and 17% amorphous carbon (10 μm). For the Shkuratov intimate model, the best fit is obtained adding some olivine, and it is composed of 13% amorphous H_2O ice (30 μm), 12% CH_3OH ice (40 μm), 20% Titan tholin (4 μm), 29% Triton tholin (4 μm), 19% amorphous carbon (10 μm), and 11% olivine (100 μm). The photometric uncertainty in the H band (Fig. 7) does not allow a more accurate model.

For detailed models and discussions on surface composition obtained for each object, as available in literature, see references reported in Table 1.

5. SURFACE COMPOSITION (STATE OF THE ART)

As discussed above, much of the information obtained from spectral modeling is nonunique, especially if the necessary conditions, as discussed above, are not met (albedo, high signal precision signatures, significant wavelength coverage, etc.). Derived abundances of different materials and even the presence of these materials are easily influenced by choices of model parameters. Nevertheless, the modeling can be used to pick out broad variations in TNO spectra.

Recently, several large objects with strong ice signatures in their spectra have been discovered. This is in contrast with the previous data, in which the majority of the objects showed spectra with faint or no ice signature (*Barucci and Peixinho,* 2006), and often with relatively low signal precision. Analyzing all the available spectra, objects are found to fall into several broad categories following those first identified by *Cruikshank et al.* (2007).

5.1. The Four Spectral Types

The aim of grouping is not to propose the following as taxonomy, but to note the basic surface characteristics of these groups. To date, four spectral groups can be identified:

1. *Methane-dominated spectra.* Most of the very largest transneptunian objects — Eris, Pluto, Sedna, and 2005 FY_9 — have infrared spectra dominated by CH_4 absorption. Some objects show spectra containing absorption bands of both CH_4 and N_2, and the CH_4 is often dissolved in the N_2 ice. Pluto and probably Sedna share these properties, together with Neptune's satellite Triton (generally thought to be a large TNO captured by Neptune). Recent modeling of Eris also seems to favor the presence of N_2 on the surface of Eris (*Merlin et al.,* 2006; *Dumas et al.,* 2007). Some other objects show spectra with absorption bands of CH_4, with clear indication that the CH_4 ice is pure and not dissolved in another ice. This is the case of 2005 FY_9. 2003 EL_{61} is the largest transneptunian object that does not have CH_4 detected on the surface. Detailed discussion of the spectra of these large TNOs can be found in the chapter by Brown.

2. *Water-ice-dominated spectra.* A number of objects have spectra that have moderate to deep absorptions due to water ice. These water ice objects include the largest objects after the methane-dominated objects, but also include smaller objects. The very deepest water-ice absorptions are found exclusively in objects dynamically similar to 2003 EL_{61}, which also has very deep water-ice absorptions. *Brown et al.* (2007) show that this dynamical cluster is consistent with being a family of collisional shards formed from a giant impact on 2003 EL_{61}. Other than this dynamical subclass for the deepest absorptions, no correlation between the presence or amount of water-ice absorption and any other factor is apparent. In particular, if the variation in water-ice absorption is interpreted as variation in the surface exposure of pure water ice with the remainder of the surface covered with red featureless tholins, we would expect to see a correlation between the color index and the water-ice absorption. Once the 2003 EL_{61}-related objects are removed, no correlation is seen. The lack of correlation between color and water-ice absorption is most likely an indication that water ice on the surfaces of these TNOs is intimately mixed with the coloring agent. The physical reason for the variation in color or the variation in water-ice absorption is nonetheless unknown.

All TNOs with spectra showing water-ice absorptions measured with sufficiently high signal precision have been shown to have the 1.65-μm feature due to the presence of crystalline water ice. This is the case for Quaoar, 2003 EL_{61}, 2002 TX_{300}, and 2003 OP_{32}. While crystalline water ice is neither expected at these temperatures nor should be stable against cosmic-ray and UV bombardment, crystalline water ice appears to be ubiquitous in the outer solar system, from the icy satellites of the giant planets, to large TNOs, to even moderate-sized satellites of TNOs (*Barkume et al.,* 2006).

The presence of crystalline water ice implies that ice has been heated to temperatures above 100/110 K. This heating could have occurred in only the uppermost layers by impacts or in the deep interiors. As discussed by *Jewitt and Luu* (2004), the presence of crystalline water could imply cryovolcanic outgassing. Complex geology, as observed on some icy satellites, indicates that solid-state convection could bring warm ices toward the surface, but the presence of crystalline water ice on even relatively small TNOs makes this suggestion appear unlikely. The quality of most of the spectra is too poor to distinguish between amorphous or crystalline water ice. Several other objects, such as Orcus (*de Bergh et al.,* 2005) and 1996 TO_{66} (*Brown et al.*, 1999), have spectra that favor the presence of crystalline water ice, although the data have relatively poor signal to signal precision. The widespread presence of crystalline water ice suggests that it is likely that some more mundane process is at work. While some objects in the outer solar system have been suggested to have a mixture of crystalline and amorphous ices (i.e., the Galilean satellites) (*Hansen and McCord,* 2004), at this point the discovery of an object with water-ice absorption that could be convincingly shown to have no crystalline water ice would be a much greater surprise.

3. *Water-ice spectra with the presence of methanol-like features.* A small number of objects show spectra with the 2.27-μm band characteristic of CH_3OH (and/or a pholotylic product of methanol). This detection suggests a chemically primitive surface, since heating and other processes remove the light hydrocarbons in favor of macromolecular carbon. The absorption band has been detected so far only on the surfaces of the TNOs 55638 2002 VE_{95} and 1998 GQ_{21} and the Centaur Pholus. Many objects have a low signal precision, especially in the K band longward of 2.2 μm, which could mask this signature. However, many objects show a decreasing slope after 2.2 μm, implying the possible presence of CH_3OH (or a similar molecule). Nonetheless, the high signal-to-noise in many spectra firmly rules out the presence of this 2.27-μm absorption at the levels seen on these three objects. The presence of methanol on the surface of some Centaurs/TNOs is taken to indicate the chemically primitive nature of these bodies. Methanol is an abundant component of many active comets and of the interstellar medium. No correlation can be found between of the other properties of the three methanol-like objects and the presence of the methanol.

4. *Featureless spectra.* Many objects have featureless spectra in the near-infrared, but a wide range of colors. Some objects are essentially neutral (gray) over this spectral interval, while others are among the reddest objects in the solar system. Geometric albedos appear to lie in the range 0.03–0.2 (see chapter by Stansberry et al.). Many spectra that appear featureless when observed at low signal precision may reveal diagnostic absorption features that place them in other groups once better spectra are available. Nonetheless, many spectra have sufficient signal-to-noise to rule out absorption due to water ice at a very low level. The spectra of this group resemble those of the dead comets and the jovian Trojans (see chapter by Dotto et al.). These bodies could have surface mantles rich in organic material or carbon (see chapter by de Bergh et al.) that mask interior ice.

5.2. Variegated Surfaces: Heterogeneity and Homogeneity

Observations of several icy satellites have shown heterogeneous surfaces due to crater formation or volcanism, which reveal fresh and bright icy components. Photometric and spectroscopic observations of several TNOs and Centaurs have recently shown rotational variability. Photometric variations as represented by the rotational lightcurve of an object depend on the object's shape, rotational properties, and surface variation. Variation of color indices can also reveal heterogeneous surface properties of an object. Spectroscopy is always the best tool to access the surface properties, and the near-infrared, where we can see vibrational harmonics of ices, is the best spectral range to observe such variation. From the visible range, two objects (2000 GN_{171} and 2000 EB_{173}) show visible variable spectra associated with detection of hydrated silicates or featureless materials. This variability is not confirmed and other observations are required (*Fornasier et al.,* 2004). *Barucci et al.* (2002a) obtained two spectra of the Centaur Thereus in the near-infrared region. Although the first one shows absorption features of H_2O ice, the second one is featureless, revealing the heterogeneous nature of its surface. This trend was confirmed by *Licandro and Pinilla-Alonso* (2005) and *Merlin et al.* (2005). Moreover, *Merlin et al.* (2005), using the rotational period of this object, showed the relation between the rotation phase and the presence of water ice in new near-infrared spectra. They assumed that only part of this Centaur is covered by water ice. Available observations of additional Centaurs and TNOs shows that several objects present variations of their surface properties. These include 31824 Elatus (*Bauer et al.,* 2002) and 19308 1996 TO_{66} (*Brown et al.,* 1999). In some cases, observed surface variations may be attributed to different viewing geometry, and possibly to the low signal precision of some of the observational data, in which case it is mandatory to check with higher-quality data. The partial resurfacing by nondisruptive collisions and/or activity would be the most likely cause of the heterogeneity of these objects.

5.3. Causes of the Spectral Types

To investigate the presence of ices on the whole population and the possible connection with the evolution of the TNOs, *Barucci et al.* (2006) analyzed all the NIR spectra available in the literature for which a surface compositional model was performed. No correlation was found between the taxonomic groups and the presence of ices on the surfaces. All four groups show the presence of ices. The majority of

nonicy bodies seem concentrated on the reddest group (RR) where organic compounds (causing red slopes) could hide ices present on the surface. The majority of neutral spectra (BB group) bodies have objects for which the content of ice seems generally higher than in the other groups. Similar results have been found by Barkume et al. (in preparation), analyzing the H_2O absorption depth vs. the visible gradient.

Barucci et al. (2006) investigated whether there is a connection between the presence of ice and the size of the objects. They reported that all large objects have ices detected on their surface, while smaller objects can have no ice detection (mantled bodies) or limited ice detection (see Fig. 8).

The presence of methane and other volatiles on the largest TNOs can be understood as a consequence of atmospheric retention by these bodies (see chapters by Brown and by Stern and Trafton). The vast majority of the objects in the Kuiper belt are far too small to have sufficient gravity to retain any volatile species on their surfaces, so we should expect nothing but water ice or involatile long-chain hydrocarbons or tholins on the surface.

While this general expectation is met (with the exception of the methanol-like spectra), the essentially stochastic variation in optical color and in water ice absorption is inexplicable. As a first guess, the spectra of TNOs would be expected to resemble the dark-red featureless spectra of extinct comets and primitive asteroids. While some spectra do indeed resemble these other types of objects, many do not. Some look much more like the icy satellites of the giant planets instead.

While no general explanation for the spectral variation is yet forthcoming, only a small number of possibilities appear to exist. The variations must be due to either variation in the initial composition of the objects or in variation in the subsequent history. While the Kuiper belt itself occupies too small a range in relative heliocentric distance ($\Delta a/a \sim 0.15$) to imagine large temperature or chemical gradients across it, the objects that are now in the Kuiper belt are thought to have come from a large swath of the outer solar system (see chapter by Morbidelli et al.). Indeed, the most homogeneous appearing population within the Kuiper belt, the uniformly red cold classical objects (*Morbidelli and Brown,* 2004), are potentially the only population that is relatively unperturbed. The main chemical variations that could be imagined to affect the final spectrum would be the inclusion or exclusion of hydrocarbons, which would eventually become dark and red. In general, however, the absence of any correlation between water-ice absorption and color does not strongly support this idea.

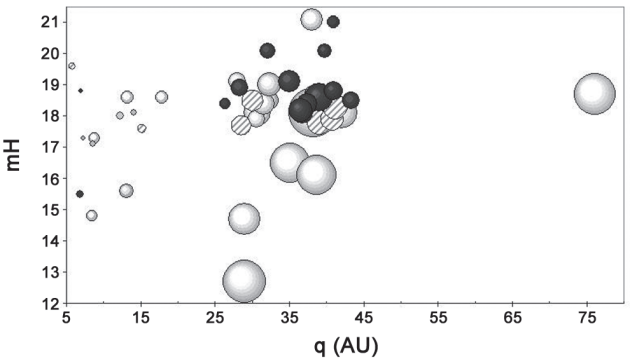

Fig. 8. Distribution of the icy (white) and nonicy (black) bodies (see Table 1) on a plot of the apparent H-band magnitude (mH) at the time of the spectral observation vs. perihelion distance. The objects with no firm detection of ices are reported with dashed lines. The size of the points is proportional to the estimated diameter of the bodies. The smaller points represent the objects with estimated diameters of ~50 km, while the biggest is for Eris, ~2500 km.

Variations in the history of the objects could also lead to spectral variations. The stochastic-appearing variations in the spectral properties of the objects make a stochastic process such as impacts an appealing possibility. Early suggestions that recent impacts might excavate fresh ices and cover red tholin-like material leading to color variations appear not to be born out. In particular, such a process would again lead to a general correlation between water-ice absorption depth and color, which is not seen, in addition to frequent rotational color and spectral variation, which has rarely been observed. While none of the explanations for the color and spectral variation of TNOs is particularly satisfying, few other general ideas seem plausible.

6. CONCLUSIONS

In this chapter we presented the knowledge of the composition of the TNO and Centaur population deduced from the different ground- and space-based spectroscopic surveys and the methods commonly used to analyze the resulting data. Surface structure plays an important role on the interpretation of V-NIR and far-infrared data. The knowledge of the surface properties doubtlessly provides constraints on the formation and evolution processes that have affected the population. The spectral behavior of objects within this population shows large differences from one another. Interpretation of these spectra is in general difficult because models of the spectra depend on the choice of many parameters (see section 4). Nevertheless, this is the best way we have to investigate their surface compositions. No correlation has been found between the presence of ice, absorption depth, taxonomic classes, and/or visible spectral gradient. The BB group seems to have objects showing more ice content on their surface. This trend may be influenced by the identification by *Brown et al.* (2007) of a possible family for which they note a correlation between strong water content and a dynamical cluster. They proposed that a giant impact on 2003 EL_{61} could have ejected a large fraction of its original mantle and formed its multiple satellite system and could also have ejected fragments of the original mantle in a clustered dynamical zone. Barkume et al. (in prepa-

ration) have shown that 65% of TNOs in their observed sample (which was not restricted to the dynamical cluster) show no definitive absorptions due to water ice. This is represented in Fig. 2 for the objects 2003 VS_2 and 1996 TP_{66}, in which the poorer signal precision may hide small signatures. No correlations have been found between ice abundance and perihelion distance.

The results presented herein also show that all large objects have the presence of some ices on their surface. This indicates that space weathering and collisional resurfacing are not the only mechanisms that can explain the surface properties and composition. It is clear that the largest TNOs can retain materials of higher albedo (ice or frost), but they can also have an outgassing from the interior. A thin atmosphere could be formed around some of these objects, as is the case for Pluto, with seasonal sublimation and recondensation of the most volatile species that would lead to surface modifications.

The variety of surface compositions among TNOs has often been attributed to different collisional evolution states and/or different degrees of surface alteration due to space weathering. In fact, it is known from laboratory experiments (chapter by Hudson et al.; *Brunetto et al.,* 2006) that bombardment by high-energy radiation of ices produces an "irradiation mantle" that is hydrogen-poor and carbon-rich, reddens the spectra, and destroys the ices' bands. If space weathering is the agent of the formation of a mantle, which hides the presence of ices on the surface, this process does not appear to work on the larger objects and other mechanisms have to be investigated.

The lack of correlation between color and water-ice absorption is most likely an indication that water ice on the surfaces of these TNOs is intimately mixed with the coloring agent. The physical reason for the variation in color or the variation in water-ice absorption is nonetheless unknown. Some methanol-like spectra exist, and this implies a chemically primitive nature for these objects, although it is not clear why only these three specific objects show methanol. Energetic impacts have certainly played an important role on the history of this population and may be the cause of at least some of the compositional surface variations.

This field benefits from continuous new discoveries. The investigation of the surface properties of TNOs is still relatively recent and its evolution will depend on the telescopes and instrumentation. A new large program is just started at VLT-ESO to observe an extended sample of objects with higher spectral quality. To investigate the surface of this faint population, albedo remains one of the fundamental parameters to be determined with accuracy. More accurate optical constants are also necessary.

In the future, the James Webb Space Telescope promises to further the exploration of TNOs and Centaurs from space (see chapter by Stansberry et al.). A possible extended mission for New Horizons (see chapter by Weaver et al.), after its encounter with Pluto in 2015, is to fly by one or more TNOs. Such an extended mission would be an exciting opportunity for an up-close look at samples of this population, providing ground truth for the results summarized in this chapter.

REFERENCES

Altenhoff W. J., Bertoldi F., and Menten K. M. (2004) Size estimates of some optically bright KBOs. *Astron. Astrophys., 415,* 771–775.

Barkume K. M., Brown M. E., and Shaller E. L. (2006) Water ice on the satellite of Kuiper belt object 2003 EL61. *Astrophys. J. Lett., 640,* L87–L89.

Barucci M. A. and Peixinho N. (2006) Trans-Neptunian objects' surface properties. In *Asteroids, Comets, and Meteors* (D. Lazzaro et al., eds.), pp. 171–190. IAU Symposium No. 229.

Barucci M. A., de Bergh C., Cuby J. G., Le Bras A., Schmitt B., and Romon J. (2000) Infrared spectroscopy of the Centaurs 8405 Asbolus: First observation at ESO-VLT. *Astron. Astrophys., 357,* L53–L56.

Barucci M. A., Boehnhardt H., Dotto E., Doressoundiram A., Romon J., Lazzarin M., Fornasier S., de Bergh C., Tozzi G. P., Delsanti A., Hainaut O., Barrera L., Birkle K., Meech K., Ortiz J. L., Sekiguchi T., Thomas N., Watanabe J., West R. M., and Davies J. K. (2002a) Visible and near-infrared spectroscopy of the Centaur 32532 (2001 PT_{13}). ESO Large Programme on Trans-Neptunian Objects and Centaurs: First spectroscopy results. *Astron. Astrophys., 392,* 335–339.

Barucci M. A., Cruikshank D. P., Mottola S., and Lazzarin M. (2002b) Physical properties of Trojan and Centaur asteroids. In *Asteroids III* (W. F. Bottke Jr. et al., eds.), p. 273. Univ. of Arizona, Tucson.

Barucci M. A., Dotto E., Brucato J. R., Muller T. G., Morris P., Doressoundiram A., Fulchignoni M., De Sanctis M. C., Owen T., Crovisier J., Le Bras A., Colangeli L., and Mennella B. (2002c) 10 Hygiea: ISO infrared observations. *Icarus, 156,* 202–210.

Barucci M. A., Cruikshank D. P., Dotto E., Merlin F., Poulet F., Dalle Ore C., Fornasier S., and de Bergh C. (2005a) Is Sedna another Triton. *Astron. Astrophys., 439,* L1–L4.

Barucci M. A., Belskaya I. N., Fulchignoni M., and Birlan M. (2005b) Taxonomy of Centaurs and Trans-Neptunian objects. *Astron. J., 130,* 1291–1298.

Barucci M. A., Merlin F., Dotto E., Doressoundiram A., and de Bergh C. (2006) TNO surface ices. Observations of the TNO 55638 (2002 V395) and analysis of the population's spectral properties. *Astron. Astrophys., 455,* 725–730.

Bauer J. M., Meech K. J., Fernández Y. R., Farnham T. L., and Roush T. L. (2002) Observations of the Centaur 1999 UG_5: Evidence of a unique outer solar system surface. *Publ. Astron. Soc. Pac., 114,* 1309–1321.

Bertoldi F., Altenhoff W., Weiss A., Menten K. M., and Albrecht M. (2006) The trans-neptunian object UB313 is larger than Pluto. *Nature, 439,* 563–564.

Boehnhardt H., Bagnulo S., Muinonen K., Barucci M. A., Kolokolova L., et al. (2004) Surface characterization of 28978 Ixion (2001 KX76). *Astron. Astrophys., 415,* L21–L25.

Brown M. E. (2000) Near-Infrared spectroscopy of Centaurs and irregular satellites. *Astron. J., 119,* 977–983.

Brown M. E. (2003) The composition of Kuiper belt objects. *Bull. Am. Astron. Soc., 35,* 969.

Brown M. E. and Calvin W. M. (2000) Evidence for crystalline water and ammonia ices on Pluto's satellite Charon. *Science, 287,* 107–109.

Brown M. E. and Koresko C. C. (1998) Detection of water ice on the Centaur 1997 CU26. *Astrophys. J. Lett., 505,* L65–L67.

Brown M. E. and Trujillo C. (2004) Direct measurement of the size of the large Kuiper belt object (50000) Quaoar. *Astrophys. J., 127,* 2413–2417.

Brown M. E., Blake G. A., and Kessler J. E. (2000) Near-infrared spectroscopy of the bright Kuiper belt object 2000 EB173. *Astrophys. J. Lett., 543,* L163–L165.

Brown M. E., Trujillo C., and Rabinowitz D. L. (2005) Discovery of a planetary-sized object in the scattered Kuiper belt. *Astrophys. J. Lett., 635,* L97–L100.

Brown M. E., Schaller E. L., Roe H. G., Rabinovitz D. L., and Trujillo C. A. (2006) Direct measurement of the size of 2003 UB313 from the Hubble Space telescope. *Astrophys. J. Lett., 643,* L61–L63.

Brown M. E., Barkume K. M., Ragozzine D., and Schaller E. L. (2007) A collisional family of icy objects in the Kuiper belt. *Nature, 446,* 294–296.

Brown R. H., Cruikshank D. P., and Pendleton Y. (1997) Surface composition of Kuiper belt object 1993 SC. *Science, 276,* 973–939.

Brown R. H., Cruikshank D. P., and Pendleton Y. (1999) Water ice on Kuiper belt object 1996 TO66. *Astron. J. Lett., 519,* L101–L104.

Brunetto R., Barucci M. A., Dotto E., and Strazulla G. (2006) Ion Irradiation of frozen methanol, methane and benzene: Linking to the colors of Centaurs and Trans-Neptunian objects. *Astrophys. J., 644,* 646.

Chandrasekhar S. (1960) *Radiative Transfer.* Dover, New York.

Choi Y. J. and Weissman P. R. (2006) *IAU Circular No. 8656*.

Christensen P. R., Bandfield J. L., Hamilton V. E., Howard D. A., Lane M. D., Piatek J. L., Ruff S. W., and Stefanov W. L. (2000) A thermal emission spectral library of rock forming minerals. *J. Geophys. Res., 105(E4),* 9735–9739.

Cooper B. L., Salisbury J. W., Killen R. M., and Potter A. E. (2002) Mid-infrared spectral features of rocks and their powders. *J. Geophys. Res., 107(E4),* 1–12.

Cruikshank D. P., Roush T. L., Bartholomew M. J., Geballe T. R., Pendleton Y. J., White S. M., Bell J. F. III, Davies J. K., Owen T. C., de Bergh C., Tholes D. I., Bernstein M. P., Brown R. H., Tryka K. A., and Dalle Ore C. M. (1998) The composition of Centaur 5145 Pholus. *Icarus, 135,* 389–407.

Cruikshank D. P., Dalle Ore C. M., Roush T. L., Geballe T. R., Owen T. C., de Bergh C., Cash M. D., and Hartmann W. K. (2001) Constraints on the composition of Trojan asteroid 624 Hektor. *Icarus, 153,* 348–360.

Cruikshank D. P., Stansberry J. A., Emery J. P., Fernández Y. R., Werner M. W., et al. (2005) The high albedo Kuiper object (55565) 2002 AW197. *Astrophys. J. Lett., 624,* L53–L56.

Cruikshank D. P., Barucci M. A., Emery J. P., Fernández Y. R., Grundy W. M., Noll K. S., and Stansberry J. A. (2007) Physical properties of trans-Neptunian objects. In *Protostars and Planets V* (B. Reipurth et al., eds.), pp. 879–893. Univ. of Arizona, Tucson.

de Bergh C., Boehnhardt H., Barucci M. A., Lazzarin M., Fornasier S., Romon-Martin J., Tozzi G. P., Doressoundiram A., and Dotto E. (2004) Aqueous altered silicates in the surface of two Plutinos? *Astron. Astrophys., 416,* 791–798.

de Bergh C., Delsanti A., Tozzi G. P., Dotto E., Doressoundiram A., and Barucci M. A. (2005) The surface of the trans-Neptunian object 90482 Orcus. *Astron. Astrophys., 437,* 1115–1120.

Doressoundiram A., Tozzi G. P., Barucci M. A., Boehnhardt H., Fornasier S., Romon J. (2003) ESO Large Programme on Trans-Neptunian Objects and Centaurs: Spectroscopic investigation of Centaur 2001 BL41 and TNOs (26181) 1996 GQ21 and 26375 1999 DE9. *Astron. J., 125,* 2721–2727.

Doressoundiram A., Barucci M. A., Tozzi G. P., Poulet F., Boehnhardt H., de Bergh C., and Peixinho N. (2005) Spectral characteristics and modelling of the trans-Neptunian object (55565) 2002 AW197 and the Centaurs (55576) 2002 GB10 and (83982) 2002 GO9. *Planet. Space Sci., 53,* 1501–1509.

Dotto E., Barucci M. A., Müller T. G., Brucato J. R., Fulchignoni M., Mennella V., and Colangeli L. (2002) ISO observations of low and moderate albedo asteroids: PHT-P and PHT-S results. *Astron. Astrophys., 393,* 1065–1072.

Dotto E., Barucci M. A., Boehnhardt H., Romon J., Doressoundiram A., Peixinho N., de Bergh C., and Lazzarin M. (2003a) ESO Large Programme on Trans-Neptunian Objects and Centaurs: Searching for water ice on 47171 1999 TC36, 1998 SG35, and 2000 QC243. *Icarus, 162,* 408–414.

Dotto E., Barucci M. A., Leyrat C., Romon J., de Bergh C., and Licandro J. (2003b) Unveiling the nature of 10199 Chariklo: Near-infrared observations and modelling. *Icarus, 164,* 122–126.

Dotto E., Barucci M. A., Brucato J. R., Müller T. G., and Carvano J. (2004) Polyxo: ISO-SWS spectrum up to 26 micron. *Astron. Astrophys., 427,* 1081–1084.

Doute S. and Shmitt B. (1998) A multilayer bidirectional reflectance model for the analysis of planetary surface hyperspectral images at visible and near-infrared wavelengths. *J. Geophys. Res., 103(E13),* 31367–31390.

Doute S., Schmitt B., Quirico E., Owen T. C., Cruikshank D. P., de Bergh C., Geballe T. R., and Roush T. L. (1999) Evidence for methane segregation at the surface of Pluto. *Icarus, 142,* 421–444.

Dumas C., Hainault O., Merlin F., Barucci M. A., de Bergh C., Guilbert A., Vernazza P., and Doressoundiram A. (2007) Surface composition of the largest Dwarf Planet 136199 Eris (2003 UB313). *Astron. Astrophys., 471,* 331–334.

Emery J. P. and Brown R. H. (2004) The surface composition of Trojan asteroids: Constraints set by scattering theory. *Icarus, 170,* 131–152.

Emery J. P., Cruikshank D. P., and Van Cleve J. (2006) Thermal emission spectroscopy (5.2–38 μm) of three Trojan asteroids with the Spitzer Space Telescope: Detection of fine-grained silicates. *Icarus, 182,* 496–512.

Fernandez Y. R., and 9 colleagues (2001) *IAU Circular No. 7689,* 3.

Fernandez Y. R., Jewitt D. C., and Sheppard S. S. (2002) Thermal properties of Centaurs Asbolus and Chiron. *Astron. J., 123,* 1050–1055.

Fornasier S., Dotto E., Barucci M. A., and Barbieri C. (2004a) Water ice on the surface of the large TNO 2004 DW. *Astron. Astrophys., 422,* L43–L46.

Fornasier S., Doressoundiram A., Tozzi G. P., Barucci M. A., Boehnhardt H., de Bergh C., Delsanti A., Davies J., and Dotto E. (2004b) ESO Large Programme on Trans-Neptunian Objects and Centaurs: Final results of the visible spectrophotometric observations. *Astron. Astrophys., 421,* 353–363.

Foster M. J., Green S. F., McBride N., and Davies J. K. (1999)

Detection of water ice on 2060 Chiron. *Icarus, 141,* 408–410.
Grundy W. M. and Fink U. (1996) Synoptic CCD spectrophotometry of Pluto over the past 15 years. *Icarus, 124,* 329–343.
Grundy W. M. and Schmitt B. (1998) The temperature-dependent near-infrared absorption spectrum of hexagonal H_2O ice. *J. Geophys. Res., 103(E11),* 25809–25822.
Grundy W. M., Buie M. W., and Spencer J. R. (2005) Near-infrared spectrum of low-inclination classical Kuiper belt object (79360) 1997 CS_{29}. *Astron. J., 130,* 1299–1301.
Gulbis A. A. S., Elliot J. L., Person M. J., Adams E. R., Babcock B. A., et al. (2006) Charon's radius and atmospheric constraints from observations of a stellar occultation. *Nature, 439,* 48–51.
Hansen G. B. and McCord T. B. (2004) Amorphous and crystalline ice on the Galilean satellites: A balance between thermal and radiolytic processes. *J. Geophys. Res., 109,* E01012, 1–19.
Hapke B. (1966) An improved lunar theoretical photometric function. *Astron. J., 71,* 333–339.
Hapke B. (1981) Bidirectional reflectance spectroscopy I, Theory. *J. Geophys. Res., 86(B4),* 3039–3054.
Hapke B. (1984) Bidirectional reflectance spectroscopy III, Correction for macroscopic roughness. *Icarus, 59,* 41–59.
Hapke B. (1986) Bidirectional reflectance spectroscopy IV, The extinction coefficient and the opposition effect. *Icarus, 67,* 264–280.
Hapke B. (1996) A model of radiative and conductive energy transfer in planetary regoliths. *J. Geophys. Res., 101(E7),* 16817–16831.
Hapke B. and Wells E. (1981) Bidirectional reflectance spectroscopy II, Experiments and observations. *J. Geophys. Res., 86(B4),* 3055–3060.
Hapke B., Dimucci D., Nelson R., and Smythe W. (1997) Bidirectional reflectances of regoliths with grain sizes of the order of the wavelength (abstract). In *Lunar and Planetary Science XXVIII,* pp. 513–514.
Henyey C. and Greenstein J. (1941) Diffuse radiation in the galaxy. *Astron. J., 93,* 70–83.
Houck J. and 34 colleagues (2004) The Infrared Spectrograph on the Spitzer Space Telescope. *Astrophys. J. Suppl. Ser., 154,* 18–24.
Jewitt D. and Luu J. (2001) Colors and spectra of Kuiper belt objects. *Astron. J., 122,* 2099–2114.
Jewitt D. and Luu J. (2004) Crystalline water ice on the Kuiper belt object (50000) Quaoar. *Nature, 432,* 731–733.
Kern S. D., McCarthy D. W., Buie M. W., Brown R. H., Campins H., and Rieke M. R. (2000) Compositional variation on the surface of Centaur 8405 Asbolus. *Astrophys. J., 542,* L155–L159.
Lazzarin M., Barucci M. A., Boehnhardt H., Tozzi G. P., de Bergh C., and Dotto E. (2003) ESO Large Programme on Physical Studies of Trans-Neptunian Objects and Centaurs: Visible spectroscopy. *Astron. J., 125,* 1554–1558.
Licandro J. and Pinilla-Alonso N. (2005) The inhomogeneous surface of Centaur 32522 Thereus (2001 PT_{13}). *Astrophys. J., 630,* L93–L96.
Licandro J., Oliva E., and Di Martino M. (2001) NICS-TNG infrared spectroscopy of trans-neptunian 2000 EB173 and 2000 WR106. *Astron. Astrophys., 373,* L29–L32.
Licandro J., Ghinassi F., and Testi L. (2002) Infrared spectroscopy of the largest known trans-Neptunian object 2001 KX_{75}. *Astron. Astrophys., 388,* L9–L12.
Licandro J., Pinilla-Alonso N., Pedani M., Oliva G., Tozzi G., and Grundy W. (2006a) Methane ice rich surface of large TNO 2005 FY9. *Astron. Astrophys., 445,* L35–L38.
Licandro J., di Fabrizio L., Pinilla-Alonso N., de Leon J., and Oliva E. (2006b) Trans-Neptunian object (55636) 2002 TX300, a fresh icy surface in the outer solar system. *Astron. Astrophys., 457,* 329–333.
Luu J. X. and Jewitt D. C. (1990) Cometary activity in 2001 Chiron. *Astron. J., 100,* 913–932.
Luu J. and Jewitt D. (1996) Color diversity among the Centaurs and Kuiper belt objects. *Astron. J., 112,* 2310.
Luu J. and Jewitt D. (1998) Optical and infrared reflectance spectrum of Kuiper belt object 1996 TL66. *Astrophys. J. Lett., 494,* L117–L120.
Luu J., Jewitt D., and Trujillo C. (2000) Water ice in 2060 Chiron and its implications for Centaurs and Kuiper belt objects. *Astrophys. J. Lett., 531,* L151–L154.
Merlin F., Barucci M. A., Dotto E., de Bergh C., and Lo Curto G. (2005) Search for surface variations on TNO 47171 and Centaur 32532. *Astron. Astrophys., 444,* 977–982.
Merlin F., Dumas C., Barucci M. A., Hainaut O., de Bergh C., and Guilbert A. (2006) Spectroscopic analysis of the bright TNOs 2003 UB_{313} and 2003 EL_{61}. *Bull. Am. Astron. Soc., 38,* 556.
Millis R. L., Wasserman L. H., Franz O. G., Nye R. A., Elliot J. L., Dunham E. W., Bosh A. S., Young L. A., Silvan S. M., and Gilmore A. C. (1993) Pluto's radius and atmosphere — Results from the entire 9 June 1988 occultation data set. *Icarus, 105,* 282–297.
Mishchenko M. I. (1994) Asymmetry parameters of the phase function for densely packed scattering grains. *J. Quant. Spectros. Rad. Trans., 52,* 95–110.
Morbidelli A. and Brown M. (2004) The Kuiper belt and the primordial evolution of the solar system. In *Comets II* (M. C. Festou et al., eds.), pp. 175–192. Univ. of Arizona, Tucson.
Noll K. S., Luu J., and Gilmore D. (2000). Spectrophotometry of four Kuiper belt objects with NICMOS. *Astron. J., 119,* 970–976.
Owen T. C., Roush T. L., Cruikshnak D. P., Elliot J. L., Young L. A., de Bergh C., Schmitt B., Geballe T. R., Brown R. H., and Bartholomew M. J. (1993) Surface ices and the atmospheric composition of Pluto. *Science, 261,* 745–748.
Piatek J. L., Hapke B., Nelson R. M., Hale A. S., and Smythe W. D. (2003) Size-dependent measurements of the scattering properties of planetary regolith analogs: A challenge to theory (abstract). In *Lunar and Planetary Science XXXIV,* Abstract #1440.
Poulet F., Cuzzi J. N., Cruikshank D. P., Roush T. and Dalle Ore C. M. (2002) Comparison between the Shkuratov and Hapke scattering theories for solid planetary surfaces: Application to the surface composition of two Centaurs. *Icarus, 160,* 313–324.
Pravdo S., Helim E. F., Hicks M., and Lawrence K. (2001) *IAU Circular No. 7738.*
Press W. H., Flannery B. P., Teulolsky S. A., and Vetterling W. T. (1986) *Numerical Recipes.* Cambridge Univ., Cambridge.
Quirico E., Doute S., Schmitt B., de Bergh C., Cruikshank D. P, Owen T. C., Geballe T. R., and Roush T. L. (1999) Composition state and distribution of ices at the surface of Triton. *Icarus, 139,* 159–178.
Rabinowitz D. L., Barkume K., Brown M. E., Roe H., Schawartz M., Tourtellotte S., and Trujillo C. (2006) Photometric obser-

vations constraining the size, shape, and albedo of 2003 EL61, a rapidly rotating, Pluto sized object in the Kuiper belt. *Astrophys. J., 639,* 1238–1251.

Romon-Martin J., Barucci M. A., de Bergh C., Doressoundiram A., Peixinho N., and Poulet F. (2002) Observations of Centaur 8405 Asbolus: Searching for water ice. *Icarus, 160,* 59–65.

Romon-Martin J., Delahodde C., Barucci M. A., de Bergh C., and Peixinho N. (2003) Photometric and spectroscopic observations of (2060) Chiron at the ESO Very Large Telescope. *Astron. Astrophys., 400,* 369–373.

Salisbury J. W., Walter L. S., Vergo N., and D'Aria D. M. (1992). *Mid-Infrared (2.1–25 μm) Spectra of Minerals*. Johns Hopkins Univ., Baltimore.

Sheppard S. S. and Jewitt D. C. (2002) Time-resolved photometry of Kuiper belt objects: Rotations, shapes, and phase functions. *Astron. J., 124,* 1757–1775.

Shkuratov Y., Starukhina L., Hoffmann H., and Arnold G. (1999) A model of spectral albedo of particulate surface: Implications for optcical properties of the moon. *Icarus, 137,* 235–246.

Sicardy B., Bellucci A., Gendro E., Lacombe F., Lacour S., et al. (2006) Charon's size and an upper limit on its atmosphere from a stellar occultation. *Nature, 439,* 52–54.

Tholen D. J. and Buie M. W. (1989) Further analysis of Pluto-Charon mutual event observations. *Bull. Am. Astron. Soc., 21,* 981.

Thomas N., Eggers S., Ip W.-H., Lichtenberg G., Fitzsimmons A., et al. (2000) Observations of the transneptunian objects 1993 SC and 1996 TL66 with the Infrared Space Observatory. *Astrophys. J., 534,* 446–455.

Trujillo C. A., Brown M. E., Rabinowitz D. L., and Geballe T. R. (2005) Near infrared surface properties of the two intrinsically brightest minor planets: (90377) Sedna and (90482) Orcus. *Astrophys. J., 627,* 1057–1065.

Trujillo C. A., Brown M. E., Barkume K. M., Schaller E. L., and Rabinowitz D. L. (2007) The surface of 2003 EL61 in the near infared. *Astrophys. J., 655,* 1172–1178.

Vilas F. and Gaffey M. J. (1989) Phyllosilicate absorption features in main-belt and outer-belt asteroid reflectance spectra. *Science, 246,* 790–792.

Werner M. W. and 25 colleagues (2004) The Spitzer Space Telescope mission. *Astrophys. J. Suppl. Ser., 154,* 1–9.

Witteborn F. C. and Roush T. L. (2000) Thermal emission spectroscopy of 1 Ceres: Evidence for olivine. In *Thermal Emission Spectroscopy and Analysis of Dust, Disks, and Regoliths* (M. L. Sitko et al., eds.), pp. 197–203. ASP Conference Series 196, Astronomical Society of the Pacific, San Francisco.